Spherical Templating of $CoSe_2$ Nanoparticle-Decorated MXenes for Lithium-Sulfur Batteries

Wei Ying Lieu[1,2], Daliang Fang[2], Yuanjian Li[1], Xue Liang Li[2], Congjian Lin[2], Anupma Thakur[3], Brian C. Wyatt[3], Shengnan Sun[1], Tanmay Ghosh[1], Babak Anasori[3], Man-Fai Ng[4], Hui Ying Yang[2], Zhi Wei Seh[1]**

[1]Institute of Materials Research and Engineering, Agency for Science, Technology and Research (A*STAR), 2 Fusionopolis Way, Innovis, Singapore 138634, Singapore

*Email: sehzw@imre.a-star.edu.sg

[2]Pillar of Engineering Product Development, Singapore University of Technology and Design, 8 Somapah Road, Singapore 487372, Singapore
*E-mail: yanghuiying@sutd.edu.sg

[3]Department of Mechanical and Energy Engineering and Integrated Nanosystems Development Institute, Purdue School of Engineering and Technology, Indiana University-Purdue University Indianapolis, Indianapolis 46202, USA

[4]Institute of High Performance Computing, Agency for Science, Technology and Research (A*STAR), 1 Fusionopolis Way, Connexis, Singapore 138632, Singapore

Keywords: Lithium-sulfur batteries, MXenes, $CoSe_2$, sulfur spheres, spherical templating.

Abstract

Two-dimensional MXenes produce competitive performances when incorporated into lithium-sulfur batteries (LSBs), solving key problems such as the poor electronic conductivity of sulfur and dissolution of its polysulfide intermediates. However, MXene nanosheets are known to easily aggregate and restack during electrode fabrication, filtration or water removal, limiting their practical applicability. Furthermore, in complex electrocatalytic reactions like the multi-step sulfur reduction process in LSBs, MXene alone is insufficient to ensure an optimal reaction pathway. In this work, we demonstrate for the first time a loose templating of sulfur spheres using $Ti_3C_2T_x$ MXene nanosheets decorated with polymorphic $CoSe_2$ nanoparticles. This work shows that the templating of sulfur spheres using nanoparticle-decorated MXene nanosheets can prevent nanosheet aggregation and exert a strong electrocatalytic effect, thereby enabling improved reaction kinetics and battery performance. The S@MXene-$CoSe_2$ cathode demonstrated a long cycle life of 1000 cycles and a low capacity decay rate of 0.06% per cycle in LSBs.

Introduction

Lithium-sulfur batteries (LSBs) are known to be a potential candidate for next-generation energy storage devices due to sulfur having a high theoretical capacity (1675 mAh/g), being environmentally benign, and being abundant in nature.[1, 2] Recently, a family of two-dimensional (2D) materials known as MXenes have been increasingly incorporated into batteries, particularly in LSBs.[1-11] Through selective etching of their parent MAX phases, MXenes are synthesised with a general formula of $M_{n+1}X_nT_x$, where M is an early transition metal (e.g., Ti, V, Nb, and Mo), X is C and/or N, T_x represents various surface termination groups (e.g., –OH, –O, and/or –F groups), and n = 1 to 4.[12, 13] As a polar 2D material, MXene is known to have excellent electrical conductivity and significant chemisorption ability towards the lithium polysulfides (LiPSs) intermediates during the sulfur reduction reaction, helping to alleviate several critical existing problems in LSBs,[4] including (1) poor electronic and ionic conductivities of sulfur and its discharged LiPSs; (2) dissolution and diffusion of LiPSs into electrolyte; and (3) sluggish reaction kinetics of insulating Li_2S during cycling.[14-22]

However, despite the potential of MXenes, their 2D layered morphology is prone to restacking or aggregation during electrode fabrication, limiting the ionic transport through the electrode and hindering the performance of the material.[6] Concerning this, it was previously shown that restacking and aggregation can be mitigated by integrating MXene nanosheets into 3D macroporous structures such as sulfur spheres through spherical templating (S@MXene), permitting significant improvements in battery performances.[23-25] Nonetheless, there are times when MXenes themselves have intrinsic limitations to fulfilling certain needs, particularly in LSBs that involve multi-step reactions. Thus, beyond the spherical templating of pure MXenes, other ways have been deployed to further functionalise MXene spheres depending on the applications.[26-29] Unfortunately, these functionalisation methods are often non-versatile, mostly involving single-atom catalysts, dopants, or growth methods that have limitations to the degree of functionalisation, imposing a ceiling on the application performance.[27] Hence, there is a crucial need to derive an effective way that integrates the functionalisation of MXenes with spherical templating.

Inspired by earlier works on nanoparticle-decorated graphene nanospheres,[30] we demonstrate that $Ti_3C_2T_x$ MXene nanosheets decorated with polymorphic $CoSe_2$ nanoparticles can conduct spherical templating, forming a loose-templating configuration on sulfur spheres (S@MXene-

$CoSe_2$).[31, 32] Differing from conventional spherical-templated MXene spheres where MXene sheets form a rigid wall, the nanosheets in loose-templated spheres drape around the internal sphere. Importantly, the presence of $CoSe_2$ nanoparticles prevents the MXene nanosheets from restacking around the internal sulfur sphere (**Figure 1**), leading to more facile ionic transport. Polymorphic $CoSe_2$ nanoparticles comprising both cubic and orthorhombic phases (previously unreported in LSBs)[33-41] were determined to be suitable for stepwise sulfur reduction reaction via density functional theory (DFT) calculations. Furthermore, polymorphic $CoSe_2$ was found to exhibit remarkable catalytic capabilities and strong chemisorption abilities towards LiPSs, resulting in improved reaction kinetics and LSB performance.

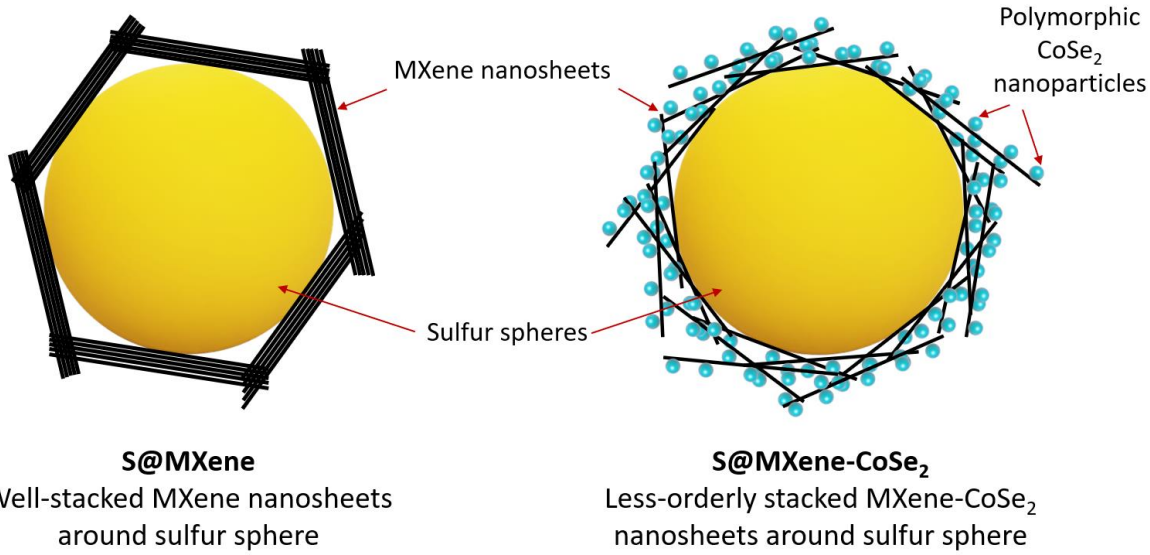

Figure 1. Schematic to demonstrate the differences in MXene nanosheet stacking for S@MXene as compared to S@MXene-$CoSe_2$.

Results and Discussion

To determine the potential of MXene-$CoSe_2$ nanosheets in LSBs, DFT calculations were first conducted to assess the nanosheets' electrocatalytic function and affinity to polysulfides.[42] Generally, $CoSe_2$ nanoparticles exist in cubic pyrite-type or orthorhombic marcasite-type structures, where the Co atoms are octahedrally bonded to the surrounding Se atoms.[43] Therefore, simulations were conducted for polysulfide adsorption for 3 different surfaces, namely orthorhombic $CoSe_2$ (O-$CoSe_2$), cubic $CoSe_2$ (C-$CoSe_2$), and $Ti_3C_2O_2$.[44, 45] $Ti_3C_2O_2$ was chosen as the passivated form of $Ti_3C_2T_x$ due to the water solvent, and mild oxidation is assumed during the synthesis process. Based on the optimised simulation model of O-$CoSe_2$ and C-$CoSe_2$, chemical interactions are dominated by the bonds formed between the S atoms in polysulfides and the Co atoms, whereas in $Ti_3C_2O_2$, the chemical interactions are dominated by the bonds between the polysulfides' Li atoms and $Ti_3C_2O_2$'s C atoms (**Figure S1**). The bonding characteristics are shown in the charge density analysis for Li_2S_6 and Li_2S molecules (**Figure 2a,b**). The charge depletion/accumulation regions indicate that there is charge transfer between the polysulfides and the surfaces, showing both short and long-chain polysulfides adsorbed stably on these surfaces. Simulation results on binding energy show that across all polysulfides, the general order of binding strength is O-$CoSe_2$>$Ti_3C_2O_2$>C-$CoSe_2$ (**Figure 2c**).

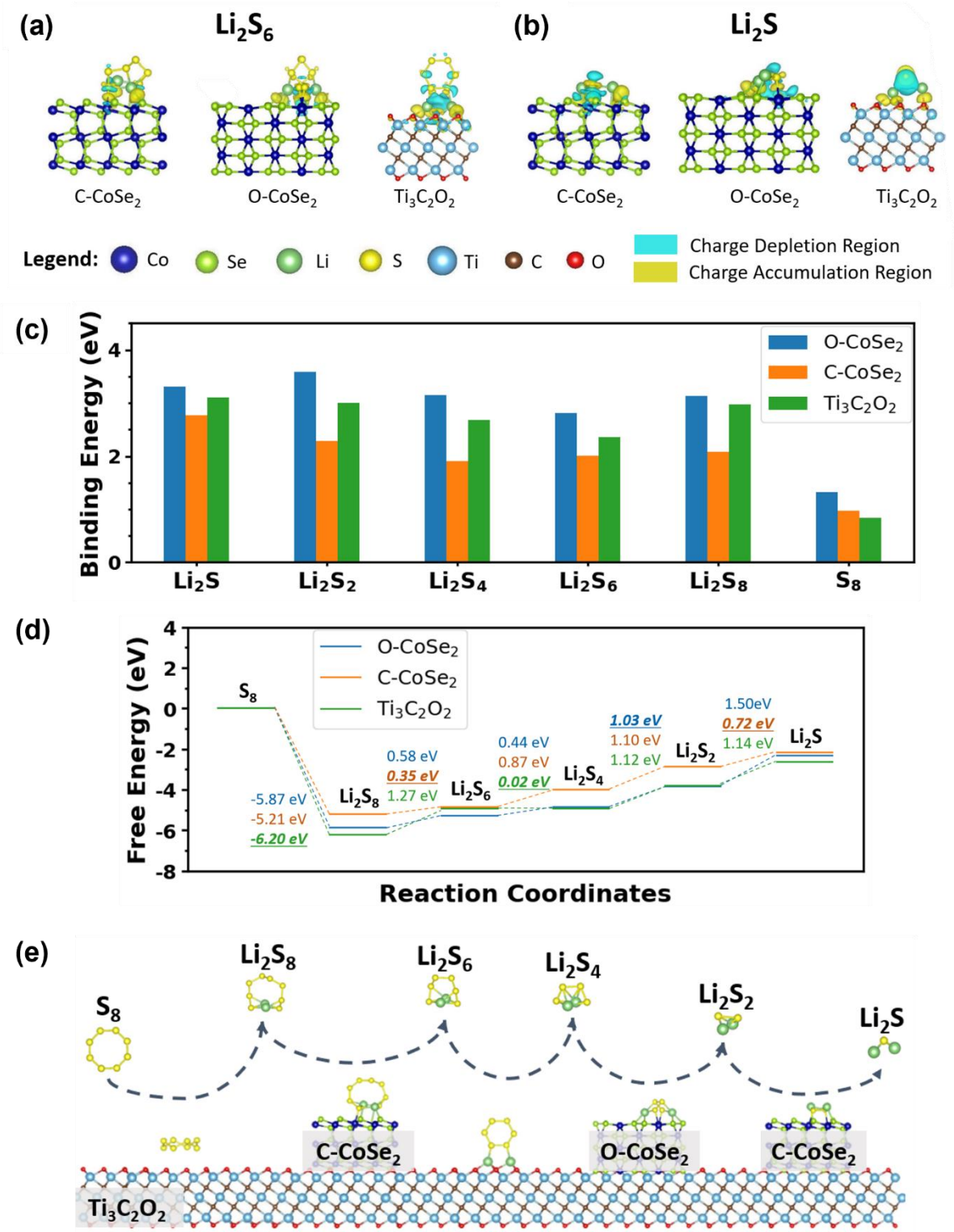

Figure 2. DFT simulations for MXene-$CoSe_2$ nanosheets. The charge density difference plots for **(a)** Li_2S_6 and **(b)** Li_2S adsorbed on C-$CoSe_2$, O-$CoSe_2$, and $Ti_3C_2O_2$. **(c)** Binding energies between lithium polysulfides and O-$CoSe_2$, C-$CoSe_2$, $Ti_3C_2O_2$ respectively. This shows that out of the 3 surfaces, O-$CoSe_2$ has the strongest binding energies for all polysulfides. **(d)** The Gibbs free energy profiles of lithium polysulfides on O-$CoSe_2$, C-$CoSe_2$, and $Ti_3C_2O_2$. The changes in energy values are colour coded according to the respective surfaces, whereas the underlined values indicate the smallest positive change for that reduction step. With each reduction step having a minimum value based on different surfaces, this Gibbs free energy profile diagram shows that MXene-$CoSe_2$ can

potentially conduct stepwise electrocatalysis. **(e)** Schematic representation of the stepwise electrocatalysis process according to the Gibbs free energy profile, in which the optimal catalytic material for each intermediate step was illustrated.

Free-energy diagrams of the progressive reaction from S_8 to Li_2S ($S_8 \rightarrow Li_2S_8 \rightarrow Li_2S_6 \rightarrow Li_2S_4 \rightarrow Li_2S_2 \rightarrow Li_2S$) were also calculated for the different materials, which allowed us to determine that stepwise electrocatalysis can occur for MXene-$CoSe_2$ nanosheets (**Figure 2d**). Based on the calculated Gibbs free energy, the reaction from S_8 to Li_2S_8 is spontaneous for all 3 materials. The C-$CoSe_2$ surface is also observed to have the optimal catalytic pathway by having the lowest overall positive change in energy from Li_2S_8 to Li_2S, with the rate-determining steps for $Ti_3C_2O_2$, C-$CoSe_2$, and O-$CoSe_2$ to be $Li_2S_8 \rightarrow Li_2S_6$, $Li_2S_4 \rightarrow Li_2S_2$, and $Li_2S_2 \rightarrow Li_2S$ respectively. As each material has a different rate-determining step, it is possible for the highly coveted stepwise electrocatalysis strategy in LSBs to occur via adsorption and desorption on different material surfaces.[46]

In previous studies, researchers have often identified the reduction of Li_2S_2 to Li_2S as the rate-determining step that causes the sluggish sulfur redox reactions.[47, 48] In this work, through the calculation of the least positive energy change, we have identified that C-$CoSe_2$ can significantly lower the $Li_2S_2 \rightarrow Li_2S$ energy change to 0.72 eV when compared to O-$CoSe_2$ (1.50 eV) and $Ti_3C_2O_2$ (1.14 eV). Similar cases of significant energy change decreases are also observed for the other intermediate steps, allowing us to determine a potential reaction pathway with the lowest energy change. This potential optimised reaction pathway is illustrated in **Figure 2e**, such that $Li_2S_8 \rightarrow Li_2S_6$, $Li_2S_6 \rightarrow Li_2S_4$, $Li_2S_4 \rightarrow Li_2S_2$, and $Li_2S_2 \rightarrow Li_2S$ have the lowest energy changes when adsorbed on C-$CoSe_2$, $Ti_3C_2O_2$, O-$CoSe_2$, and C-$CoSe_2$ respectively, providing a catalytic pathway that is more optimal than the 3 surfaces individually. Therefore, these simulation results show that MXene-$CoSe_2$ is a potentially remarkable material when used in LSBs.

MXene-$CoSe_2$ nanosheets are first synthesised through a simple gelation process by introducing Co^{2+} ions into the $Ti_3C_2T_x$ MXene dispersion **(Figure S2).**[49] The electrostatic interaction between the positive Co^{2+} ions and the negative surface functional groups of MXene permits the self-assembly formation of MXene/Co^{2+} and their sedimentation. Further selenisation of the obtained sediments by chemical vapour deposition of selenium at 300°C under argon atmospheres yielded MXene-$CoSe_2$ nanosheets.

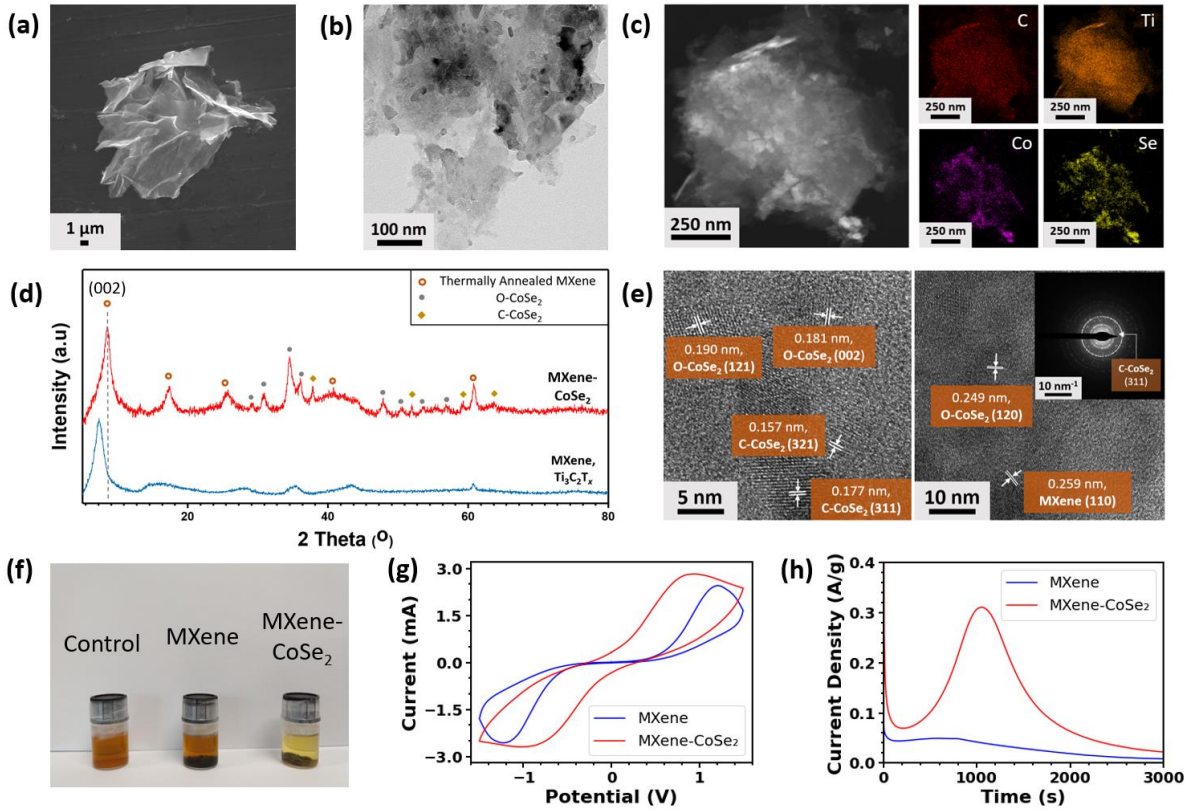

Figure 3. (a) SEM and **(b)** TEM of MXene-$CoSe_2$ nanosheets. **(c)** Elemental mapping demonstrating the distribution of nanoparticles on MXene-$CoSe_2$ nanosheets. **(d)** XRD patterns of $Ti_3C_2T_x$ MXene sheets and MXene-$CoSe_2$ nanosheets after baseline subtraction. **(e)** HRTEM images of the MXene-$CoSe_2$ sample with the associated lattice fringe spacings. The inset contains the SAED image. O-$CoSe_2$ denotes orthorhombic-type $CoSe_2$ while C-$CoSe_2$ denotes cubic-type $CoSe_2$. **(f)** Lithium polysulfide adsorption tests using Li_2S_6 solution for fixed masses of MXene and MXene-$CoSe_2$ nanosheets. **(g)** CV profiles of symmetric cells using MXene and MXene-$CoSe_2$ electrodes with Li_2S_6 at a scanning rate of 10 mV/s. **(h)** Dissolution profiles of Li_2S with MXene and MXene-$CoSe_2$ nanosheets.

Scanning electron microscopy (SEM) and transmission electron microscopy (TEM) images show that the MXene-$CoSe_2$ sample could retain the sheet-like morphology of MXenes with the presence of nanoparticles on MXene surfaces (**Figure 3a,b**). This is in comparison with the TEM images of MXene/Co^{2+} sediments, which were observed to have negligible nanoparticles as Co^{2+} ions intercalate between the MXene nanosheets (**Figure S3a**).[49] After the chemical vapour deposition of selenium, the selenium reacts with Co^{2+} ions to form the $CoSe_2$ nanoparticles. Based on the TEM images, these nanoparticles grown have an average diameter

size of 12.4±0.6 nm (**Figure S3b-e**). Energy dispersive X-ray spectroscopy (EDS) mapping of the MXene-$CoSe_2$ nanosheets presented a good distribution of Co and Se throughout the MXene nanosheets (**Figure 3c**), producing a consistent surface morphology.

To further determine the identity of MXene-$CoSe_2$ nanosheets, X-ray photoelectron spectroscopy (XPS), X-ray diffraction (XRD), high-resolution TEM (HRTEM) and selected area electron diffraction (SAED) analyses were conducted. However, the small nanoparticle sizes and relatively low amounts of $CoSe_2$ made it difficult for us to determine the identity of $CoSe_2$ through the above methods (**Figure S4**). Therefore, for characterisation purposes, we opted to increase the amounts of $CoSe_2$ grown on the MXene nanosheets by tripling the amount of $CoCl_2 \cdot 6H_2O$ added during synthesis.

The high-resolution XPS spectra of Ti 2p, Co 2p, and Se 3d were obtained based on the MXene-$CoSe_2$ sample with increased amounts of $CoSe_2$ nanoparticles (**Figure S5**).[34, 41, 50] The Ti 2p spectrum was deconvoluted and indexed to the following peaks: Ti-O (464.5 eV), Ti-C (461.9 eV and 455.42 eV), and O-Ti-O (458.7 eV). These functional groups indicate the presence of MXene, with Ti-O and O-Ti-O indicating that mild oxidation has occurred. The two fitted peaks of Co 2p at 778.3 eV and 793.6 eV belong to the Co^{3+} species, whereas the other pair of peaks at 780.8 eV and 796.9 eV belong to the Co^{2+} species. Two satellite peaks are also observed at 786.5 eV and 804 eV. The Se 3d spectrum was also deconvoluted into 2 peaks at 54.5 eV and 55.55 eV, which are assigned to Se $3d_{5/2}$ and Se $3d_{3/2}$ respectively.

From the XRD pattern, a right shift of the $Ti_3C_2T_x$ MXene's (002) characteristic peak as marked by the dotted line is observed along with the formation of polymorphic $CoSe_2$, containing both C-$CoSe_2$ and O-$CoSe_2$ (**Figure 3d**). This right shift was caused by the thermal annealing process, which decreased the interlayer spacings between the MXene sheets due to the removal of water molecules during annealing. During thermal annealing, the (002), (004), and (006) peaks of $Ti_3C_2T_x$ were observed to be more apparent, indicating that greater degree of MXene ordered occurred after thermal annealing (**Figure S6**).[51] However, after selenisation, the intensities of the (004) and (006) peaks relative to (002) decreased significantly, indicating that MXene-$CoSe_2$ nanosheets are now stacked with greater disorder. This is likely due to the introduction of $CoSe_2$ nanoparticles on the MXene nanosheets. The XRD pattern also consisted of characteristic peaks from both O-$CoSe_2$ (PDF no. 53-0499) and C-$CoSe_2$ (PDF no. 09-0234). This formation of polymorphic $CoSe_2$ containing both C-$CoSe_2$ and O-$CoSe_2$ was

expected due to the selenisation temperature of MXene-$CoSe_2$ being set at 300°C.[31] HRTEM and SAED images in **Figure 3e** further indicate the successful integration of polymorphic $CoSe_2$ on MXene flakes. Numerous lattice fringe spacings of ~0.190 nm, ~0.181 nm, and ~0.249 nm were measured to correspond accordingly to the (121), (002), and (120) planes of O-$CoSe_2$ respectively. Lattice fringe spacings of ~0.157 nm and ~0.177 nm were also determined to belong to the (321) and (311) planes of C-$CoSe_2$, while a spacing of ~0.259 nm is indexed to the (110) characteristic plane of $Ti_3C_2T_x$ MXene.

Raman spectroscopy shows the A_{1g} and A_g stretching peaks from C-$CoSe_2$ at 187 nm and 672 nm respectively as indicated by grey dotted lines (**Figure S7**).[50] In contrast, the Raman-active mode of O-$CoSe_2$ is not observed in the spectra, which aligns well with previously reported studies.[32, 52] For the initial MXene spectra, the Raman fingerprint of $Ti_3C_2T_x$ MXene is mostly located between 100 and 800 cm^{-1}.[53, 54] Based on previous studies, prominent Raman bands of 204 and 724 cm^{-1} in the initial MXene spectra can be assigned to different out-of-plane atom vibration modes, whereas vibrations from 250 to 500 cm^{-1} are assigned to in-plane vibrations of surface group atoms.[55] The intensity of these MXene bands is drastically reduced in the MXene-$CoSe_2$ spectra. No D and G bands of free carbon are observed in the initial MXene spectra, whereas obvious D and G bands are found in the final MXene-$CoSe_2$ spectra, indicating that the MXene has degraded to a certain extent after the synthesis process.[55]

LiPSs adsorption experiments using Li_2S_6 solutions were carried out on the original MXene and MXene-$CoSe_2$ nanosheets to determine the polysulfide adsorption ability of MXene-$CoSe_2$ (**Figure 3f**). MXene-$CoSe_2$ nanosheets induced greater colour intensity change after a week, which corresponded well to the previous binding energy calculations. Cyclic voltammetry (CV) experiments of symmetrical cells assembled using MXene nanosheets and MXene-$CoSe_2$ nanosheets as the respective electrodes in Li_2S_6 catholyte were also conducted at a scan rate of 10 mV s^{-1}. Based on **Figure 3g**, it is observed that the CV profile of the MXene-$CoSe_2$ symmetrical cell has higher current values than the MXene symmetrical cell for the same voltages, validating the reaction kinetics advantage of MXene-$CoSe_2$ nanosheets over MXene nanosheets. The kinetics of the solid-liquid conversion from Li_2S to soluble polysulfides was also monitored through a Li_2S dissolution experiment's potentiostatic measurements (**Figure 3h**).[56] The MXene-$CoSe_2$ cathodes resulted in a significant four-fold increase in current densities when compared to MXene cathodes. A higher capacity of 121 mAh/g is also observed for MXene-$CoSe_2$ cathodes, which is more than 4 times larger than MXene cathodes (25.6

mAh/g). These results further suggest that incorporating polymorphic $CoSe_2$ improved the reaction kinetics of MXenes in LSBs, agreeing with our initial DFT calculations.

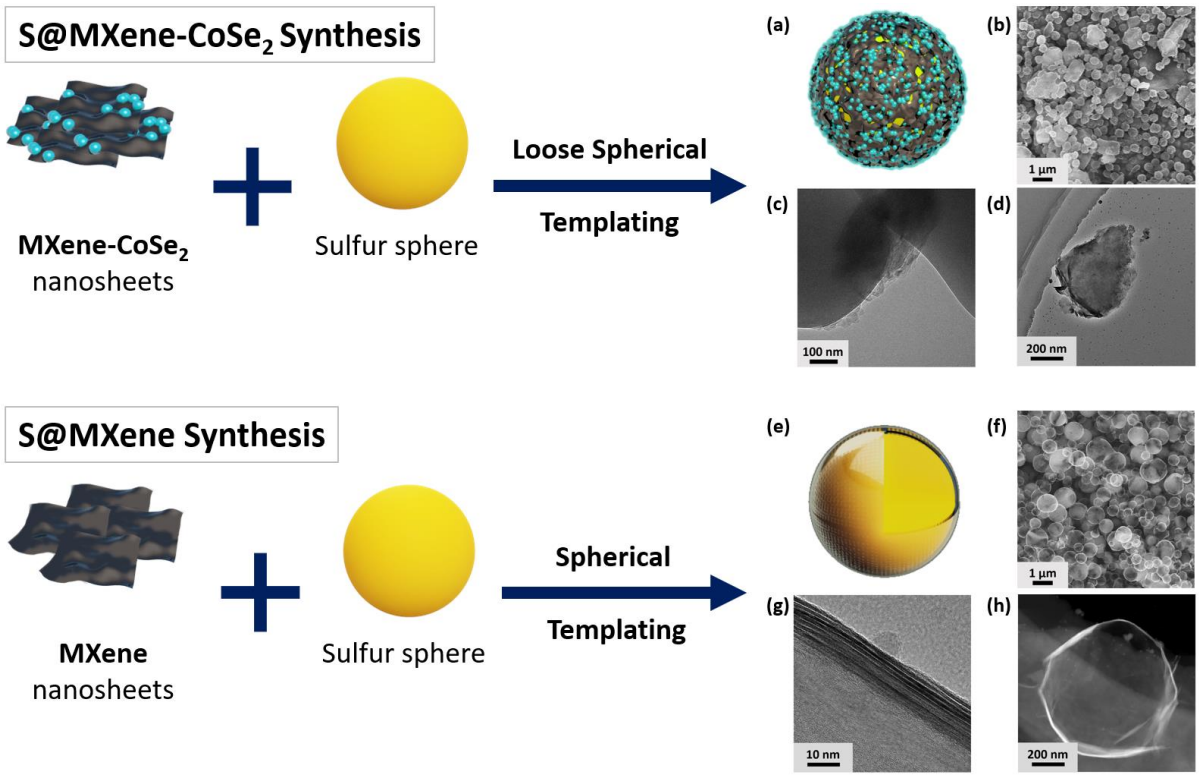

Figure 4. Schematic illustrating the differences in morphologies when sulfur spheres are wrapped with MXene-$CoSe_2$ nanosheets and MXene nanosheets. S@MXene-$CoSe_2$'s **(a)** illustration image, **(b)** SEM image, **(c)** cryo-TEM image of the external minimal restacking of MXene-$CoSe_2$ layers, and **(d)** TEM image. S@MXene's **(e)** illustration image, **(f)** SEM image, **(g)** HRTEM image of the external stacked MXene layers, and **(h)** TEM image.

Drawing inspiration from previous works on nanoparticle-decorated graphene spheres, we opted to wrap MXene-$CoSe_2$ nanosheets on sulfur spheres via spherical templating **(Figure S8)**. After sonicating for 20 min in deaerated deionised water, smaller MXene-$CoSe_2$ flakes were obtained **(Figure S9)**. These flakes were used to undergo spherical templating with sulfur spheres **(Figure S10)**. MXene flakes were also used to form S@MXene spheres in a similar process and it was observed via SEM and TEM that the S@MXene spheres have a rigid well-stacked MXene coating on the sulfur nanosphere, forming perfect spheres, whereas the S@MXene-$CoSe_2$ have an open structure, causing jagged edges or even ovoids to be observed **(Figure 4, S11)**. This open structure is attributed to MXene-$CoSe_2$ flakes having minimal stacking and not adhering strongly to the internal nanosphere, forming a loose-templated configuration.

Elemental mapping of S@MXene-$CoSe_2$ spheres indicates that substantial amounts of S, Ti, Co, and Se are still found despite the spherical templating process (**Figure S12**), showing that $CoSe_2$ nanoparticles were largely retained on the MXene nanosheets despite the process involving sonication. From the elemental mapping, the strong sulfur signal of S@MXene-$CoSe_2$ is due to its high sulfur content, similar to S@MXene spheres. Strong Ti and Se signals were also observed occasionally in regions where weak sulfur signals were observed, which might be due to the vaporisation of sulfur and the reduction of sulfur signal strength. XRD results of the S@MXene-$CoSe_2$ spheres show sharp and distinct peaks belonging to sulfur and $Ti_3C_2T_x$ MXene (**Figure S13a**), similar to the XRD of S@MXene spheres (**Figure S13b**). However, $CoSe_2$ peaks are not observed in the XRD pattern, possibly due to their small particle sizes and low content. TGA analysis also showed that the synthesised S@MXene-$CoSe_2$ and S@MXene spheres both contain ~90 wt% sulfur (**Figure S13c,d**), which confirms the incorporation of MXene-$CoSe_2$ and MXene with sulfur in both cases.

To determine the effectiveness of S@MXene and S@MXene-$CoSe_2$ spheres in LSBs, a series of electrochemical tests were conducted. Firstly, CV tests were conducted for S@MXene and S@MXene-$CoSe_2$ spheres at scanning rates from 0.1 to 0.6 mV/s to determine the Li^+ ion diffusion efficiencies (**Figure S14 and 5a**).[57] Based on the scanning rate CV tests, the peak current density at various potentials was fitted with linear graphs in **Figure 5b** according to the Randles-Sevcik equation.[5, 33, 58] A comparison of the Li^+ ion diffusion rates shows S@MXene-$CoSe_2$ spheres had a higher diffusion rate than the S@MXene spheres (**Figure S15**), indicating that improved reaction kinetics were brought about by polymorphic $CoSe_2$ nanoparticle incorporation.

Tafel analysis plots were calculated according to the first cycle of **Figure 5c** to further quantify the catalytic activity of polymorphic-$CoSe_2$. S@MXene-$CoSe_2$ spheres are characterised by lower Tafel slope values for reduction and oxidation steps, further demonstrating the enhanced reaction kinetics in both charge and discharge processes (**Figure 5d**).[59] In the initial CV profiles of S@MXene-$CoSe_2$ spheres, the two cathodic peaks at about 2.25 and 1.97 V in the first negative scan shifted to 2.27 and 2.00 V respectively before maintaining stability in the next few scans (**Figure 5c**). These 2 cathodic peaks correspond to the formation of S_8 to soluble higher-order lithium polysulfides and Li_2S respectively, while the upshifts of cathodic voltage potentials indicate decreased polarisation of S@MXene-$CoSe_2$. The consistent CV profiles in the next four cycles confirm the excellent electrochemical reversibility of S@MXene-$CoSe_2$.

Electrochemical impedance spectroscopy (EIS) of S@MXene and S@MXene-$CoSe_2$ spheres were also recorded for the batteries before cycling, and after 1, 10, and 50 cycles (**Figure S16**).[36, 60] Based on the EIS analyses, S@MXene-$CoSe_2$ delivered a lower charge-transfer resistance (13.5 Ω) than S@MXene after the 50th cycle (17.4 Ω), implying improved kinetics of polysulfide conversion through the incorporation of polymorphic $CoSe_2$.

The rate capabilities of the cells at different current densities from 0.1 to 2C (1C =1675 mA/g) were also measured. For S@MXene-$CoSe_2$ cathodes, the discharge capacities at 0.1, 0.3, 0.5, 1.0, and 2.0C are 1265, 912, 827, 750, and 669 mAh/g respectively (**Figure 5e**). In contrast, the S@MXene cathodes displayed lower discharge capacities of 1021, 697, 626, 558, and 491 mAh/g for the same current rates. Galvanostatic charge-discharge profiles of the S@MXene-$CoSe_2$ and S@MXene at various current densities from 0.1 to 2C were also presented (**Figure S17a,b**), and it is observed that the 2 discharge plateaus of S@MXene-$CoSe_2$ are still maintained even at a current density of 2C, indicating rapid polysulfide conversion reactions.

Thereafter, we defined Q1 and Q2 as the capacity of the first and second discharge plateaus respectively (**Figure S17c**). Q1 allows us to infer the amount of soluble polysulfides created and potentially diffused to the Li metal anode, while Q2 measures how efficiently polysulfides are reduced to Li_2S.[61] Therefore, the Q2/Q1 ratio can determine the material's catalytic activity, wherein higher ratios correspond to better catalytic behaviour.[62] A comparison between the Q2/Q1 ratios of S@MXene-$CoSe_2$ and S@MXene at different current densities was conducted (**Figure 5f**), and it is observed that the ratios of S@MXene-$CoSe_2$ are well above the values from S@MXene across all tested current densities.

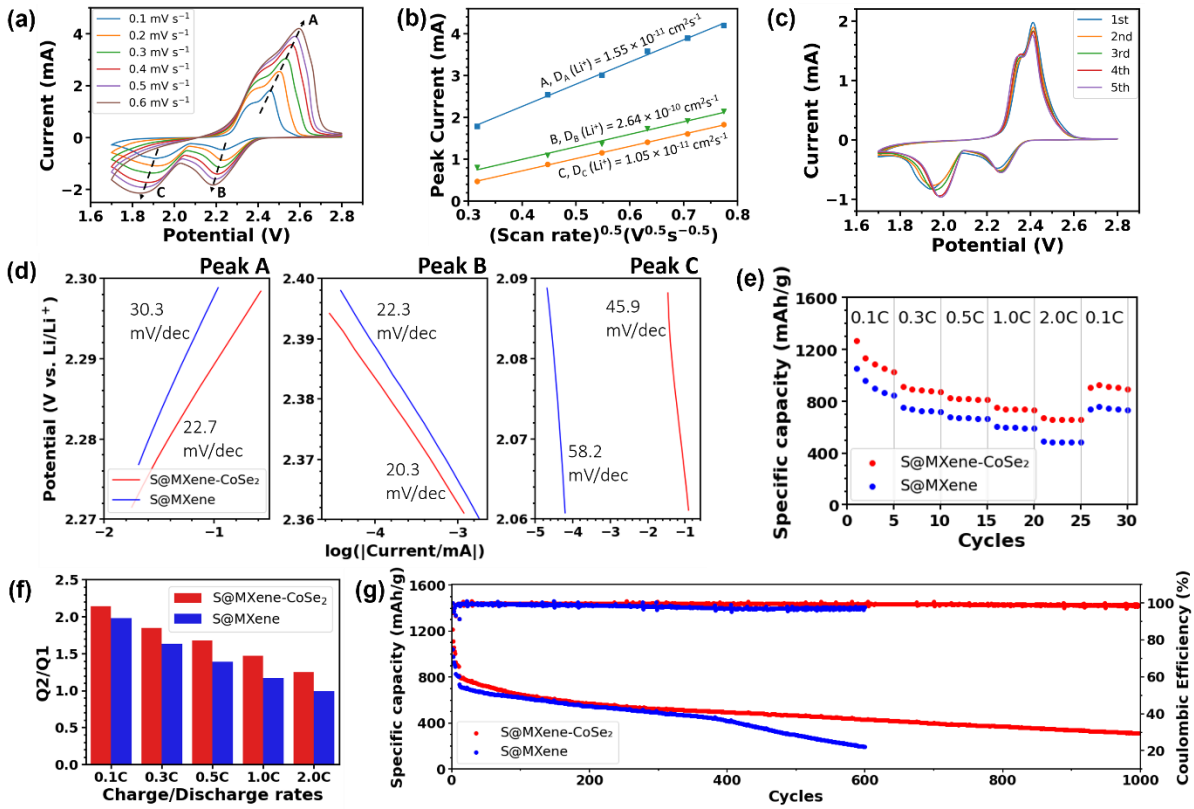

Figure 5. (a) CV curves of S@MXene-$CoSe_2$ spheres at scanning rates ranging from 0.1 to 0.6 mV/s and **(b)** the scanning rate-dependent peak currents at A, B, and C positions for the calculation of Li^+ diffusion coefficients. **(c)** Initial CV profiles of S@MXene-$CoSe_2$ spheres at a scanning rate of 0.1 mV/s. **(d)** Tafel plots of S@MXene and S@MXene-$CoSe_2$ spheres for the corresponding peak positions as derived from the CV curves. **(e)** Initial CV profiles of S@MXene-$CoSe_2$ spheres at a scanning rate of 0.1 mV/s. **(e)** Rate performance comparison of S@MXene-$CoSe_2$ and S@MXene cathodes. **(f)** Q2/Q1 ratios calculated from the charge-discharge curves for the different charge/discharge rates. **(g)** Long-term cycling performances at 0.5C of S@MXene-$CoSe_2$ and S@MXene cathodes.

The cycling performances of S@MXene-$CoSe_2$ and S@MXene cathodes at 0.5C are presented in **Figure 5g**. The S@MXene-$CoSe_2$ cathode demonstrated an initial capacity of 812 mAh/g after a low current density activation of 10 cycles and maintained a capacity of 311 mAh/g at the 1000th cycle, giving a low capacity decay rate of 0.06% per cycle. This is in contrast with the S@MXene cathode which exhibited a lower initial capacity of 736 mAh/g after low current density activation and experienced a drastic decrease in capacity around the 400th cycle, resulting in the battery performance dropping to 195 mAh/g after only 600 cycles, corresponding to a decay rate of 0.12% per cycle. This shows that the S@MXene-$CoSe_2$ cathode has much better cycling stability than the S@MXene cathode, and its performance is comparable with sulfur cathodes made using similar materials (**Table S1**). Ex-situ SEM measurements were also conducted to determine the morphological changes of the S@MXene-

$CoSe_2$ cathode during discharge and charge processes (**Figure S18**), showing superior stability of the material.

Author Contributions

W.Y. Lieu and D. Fang conceived the idea. W.Y. Lieu did most of the experiments ranging from material synthesis and electrochemical tests. W.Y. Lieu and C. Lin had lengthy discussions on material characterization. A. Thakur, B. C. Wyatt, and B. Anasori synthesised the MXenes used in this work and reviewed the manuscript. Y. Li and X. L. Li reviewed the data and the drafts of this manuscript. S. Sun and T. Ghosh conducted TEM and cryo-TEM respectively. M. Ng conducted DFT simulations and reviewed the manuscript. H. Y. Yang and Z. W. Seh supervised and reviewed the manuscript prior to submission.

Competing Interests

The authors declare no competing financial interest.

Supporting Information

Experimental details, DFT models, TEM images, XPS spectra, XRD analysis, Raman spectra, electrochemical performance graphs, TGA analysis graphs, CV graphs, EIS graphs, and galvanostatic charge and discharge profiles.

Acknowledgements

This work is supported by the Agency for Science, Technology and Research (Central Research Fund Award), and the Singapore Ministry of Education academic research grant Tier 2 (MOE2019-T2-1-181). We acknowledge the National Supercomputing Centre (NSCC) Singapore and A*STAR Computational Resource Centre (A*CRC) of Singapore through the use of its high-performance computing facilities.

References

1. Larcher, D.; Tarascon, J. M. Towards greener and more sustainable batteries for electrical energy storage. *Nat. Chem.* **2015,** 7, 19-29.
2. Bruce, P. G.; Freunberger, S. A.; Hardwick, L. J.; Tarascon, J. M. Li-O2 and Li-S batteries with high energy storage. *Nat. Mater.* **2011,** 11, 19-29.
3. Seh, Z. W.; Sun, Y.; Zhang, Q.; Cui, Y. Designing high-energy lithium-sulfur batteries. *Chem. Soc. Rev.* **2016,** 45, 5605-5634.
4. Liang, X.; Garsuch, A.; Nazar, L. F. Sulfur cathodes based on conductive MXene

nanosheets for high-performance lithium-sulfur batteries. *Angew. Chem. Int. Ed.* **2015,** 54, 3907-3911.
5. Zhang, B.; Luo, C.; Zhou, G.; Pan, Z. Z.; Ma, J.; Nishihara, H.; He, Y. B.; Kang, F.; Lv, W.; Yang, Q. H. Lamellar MXene Composite Aerogels with Sandwiched Carbon Nanotubes Enable Stable Lithium–Sulfur Batteries with a High Sulfur Loading. *Adv. Funct. Mater.* **2021,** 31, 2100793-2100802.
6. Liang, X.; Rangom, Y.; Kwok, C. Y.; Pang, Q.; Nazar, L. F. Interwoven MXene Nanosheet/Carbon-Nanotube Composites as Li-S Cathode Hosts. *Adv. Mater.* **2017,** 29, 1603040-1603047.
7. Jiang, Y.; Tian, M.; Wang, H.; Wei, C.; Sun, Z.; Rummeli, M. H.; Strasser, P.; Sun, J.; Yang, R. Mildly Oxidized MXene (Ti3C2, Nb2C, and V2C) Electrocatalyst via a Generic Strategy Enables Longevous Li-O2 Battery under a High Rate. *ACS Nano* **2021,** 15, 19640-19650.
8. Tang, H.; Li, W.; Pan, L.; Cullen, C. P.; Liu, Y.; Pakdel, A.; Long, D.; Yang, J.; McEvoy, N.; Duesberg, G. S.; Nicolosi, V.; Zhang, C. J. In Situ Formed Protective Barrier Enabled by Sulfur@Titanium Carbide (MXene) Ink for Achieving High-Capacity, Long Lifetime Li-S Batteries. *Adv. Sci.* **2018,** 5, 1800502-1800511.
9. Seh, Z. W.; Yu, J. H.; Li, W.; Hsu, P. C.; Wang, H.; Sun, Y.; Yao, H.; Zhang, Q.; Cui, Y. Two-dimensional layered transition metal disulphides for effective encapsulation of high-capacity lithium sulphide cathodes. *Nat. Commun.* **2014,** 5, 5017.
10. Zhao, Q.; Zhu, Q.; Liu, Y.; Xu, B. Status and Prospects of MXene‐Based Lithium‐Sulfur Batteries. *Adv. Funct. Mater.* **2021,** 31, 2100457-2100485.
11. Bao, W.; Liu, L.; Wang, C.; Choi, S.; Wang, D.; Wang, G. Facile Synthesis of Crumpled Nitrogen-Doped MXene Nanosheets as a New Sulfur Host for Lithium-Sulfur Batteries. *Adv. Energy Mater.* **2018,** 8, 1702485-1702496.
12. Gogotsi, Y.; Anasori, B. The Rise of MXenes. *ACS Nano* **2019,** 13, 8491-8494.
13. Naguib, M.; Kurtoglu, M.; Presser, V.; Lu, J.; Niu, J.; Heon, M.; Hultman, L.; Gogotsi, Y.; Barsoum, M. W. Two-dimensional nanocrystals produced by exfoliation of Ti3 AlC2. *Adv. Mater.* **2011,** 23, 4248-4253.
14. Manthiram, A.; Fu, Y.; Chung, S. H.; Zu, C.; Su, Y. S. Rechargeable lithium-sulfur batteries. *Chem. Rev.* **2014,** 114, 11751-11787.
15. Liu, M.; Ye, F.; Li, W.; Li, H.; Zhang, Y. Chemical routes toward long-lasting lithium/sulfur cells. *Nano Res.* **2016,** 9, 94-116.
16. Lim, W. G.; Kim, S.; Jo, C.; Lee, J. A Comprehensive Review of Materials with Catalytic Effects in Li-S Batteries: Enhanced Redox Kinetics. *Angew. Chem. Int. Ed.* **2019,** 58, 18746-18757.
17. Zhang, M.; Chen, W.; Xue, L.; Jiao, Y.; Lei, T.; Chu, J.; Huang, J.; Gong, C.; Yan, C.; Yan, Y.; Hu, Y.; Wang, X.; Xiong, J. Adsorption‐Catalysis Design in the Lithium‐Sulfur Battery. *Adv. Energy Mater.* **2019,** 10, 1903008-1903026.
18. Mikhaylik, Y. V.; Akridge, J. R. Polysulfide Shuttle Study in the Li/S Battery System. *J. Electrochem. Soc.* **2004,** 151, A1969-A1976.
19. Ji, X.; Lee, K. T.; Nazar, L. F. A highly ordered nanostructured carbon-sulphur cathode for lithium-sulphur batteries. *Nat. Mater.* **2009,** 8, 500-506.
20. Nan, C.; Lin, Z.; Liao, H.; Song, M. K.; Li, Y.; Cairns, E. J. Durable carbon-coated Li2(S) core-shell spheres for high performance lithium/sulfur cells. *J. Am. Chem. Soc.* **2014,** 136, 4659-4663.
21. Zhang, C.; Wu, H. B.; Yuan, C.; Guo, Z.; Lou, X. W. Confining sulfur in double-shelled hollow carbon spheres for lithium-sulfur batteries. *Angew. Chem. Int. Ed.* **2012,** 51, 9592-9595.
22. Lim, K. R. G.; Shekhirev, M.; Wyatt, B. C.; Anasori, B.; Gogotsi, Y.; Seh, Z. W. Fundamentals of MXene synthesis. *Nature Synthesis* **2022,** 1, 601-614.

23. Zhao, M. Q.; Xie, X.; Ren, C. E.; Makaryan, T.; Anasori, B.; Wang, G.; Gogotsi, Y. Hollow MXene Spheres and 3D Macroporous MXene Frameworks for Na-Ion Storage. *Adv. Mater.* **2017,** 29, 1702410-1702417.
24. Zhang, D.; Wang, S.; Hu, R.; Gu, J.; Cui, Y.; Li, B.; Chen, W.; Liu, C.; Shang, J.; Yang, S. Catalytic Conversion of Polysulfides on Single Atom Zinc Implanted MXene toward High‐Rate Lithium–Sulfur Batteries. *Adv. Funct. Mater.* **2020,** 30, 2002471-2002478.
25. Zhao, W.; Lei, Y.; Zhu, Y.; Wang, Q.; Zhang, F.; Dong, X.; Alshareef, H. N. Hierarchically structured Ti3C2T MXene paper for Li-S batteries with high volumetric capacity. *Nano Energy* **2021,** 86, 106120-106130.
26. Liu, Z.; Lu, D.; Wang, W.; Yue, L.; Zhu, J.; Zhao, L.; Zheng, H.; Wang, J.; Li, Y. Integrating Dually Encapsulated Si Architecture and Dense Structural Engineering for Ultrahigh Volumetric and Areal Capacity of Lithium Storage. *ACS Nano* **2022,** 16, 4642-4653.
27. Lu, C.; Li, A.; Li, G.; Yan, Y.; Zhang, M.; Yang, Q.; Zhou, W.; Guo, L. S-Decorated Porous Ti3C2 MXene Combined with In Situ Forming Cu2 Se as Effective Shuttling Interrupter in Na-Se Batteries. *Adv. Mater.* **2021,** 33, 2008414-2008427.
28. Wen, C.; Li, X.; Zhang, R.; Xu, C.; You, W.; Liu, Z.; Zhao, B.; Che, R. High-Density Anisotropy Magnetism Enhanced Microwave Absorption Performance in Ti3C2Tx MXene@Ni Microspheres. *ACS Nano* **2021,** 16, 1150-1159.
29. Wei, C.; Tian, M.; Fan, Z.; Yu, L.; Song, Y.; Yang, X.; Shi, Z.; Wang, M.; Yang, R.; Sun, J. Concurrent realization of dendrite-free anode and high-loading cathode via 3D printed N-Ti3C2 MXene framework toward advanced Li–S full batteries. *Energy Storage Mater.* **2021,** 41, 141-151.
30. Wang, H.; Yang, Y.; Liang, Y.; Robinson, J. T.; Li, Y.; Jackson, A.; Cui, Y.; Dai, H. Graphene-wrapped sulfur particles as a rechargeable lithium-sulfur battery cathode material with high capacity and cycling stability. *Nano Lett.* **2011,** 11, 2644-2647.
31. Zhang, H.; Yang, B.; Wu, X.; Li, Z.; Lei, L.; Zhang, X. Polymorphic CoSe2 with mixed orthorhombic and cubic phases for highly efficient hydrogen evolution reaction. *ACS Appl. Mater. Interfaces* **2015,** 7, 1772-1779.
32. Kong, D.; Wang, H.; Lu, Z.; Cui, Y. CoSe2 nanoparticles grown on carbon fiber paper: an efficient and stable electrocatalyst for hydrogen evolution reaction. *J. Am. Chem. Soc.* **2014,** 136, 4897-4900.
33. Cai, D.; Liu, B.; Zhu, D.; Chen, D.; Lu, M.; Cao, J.; Wang, Y.; Huang, W.; Shao, Y.; Tu, H.; Han, W. Ultrafine Co3Se4 Nanoparticles in Nitrogen‐Doped 3D Carbon Matrix for High‐Stable and Long‐Cycle‐Life Lithium Sulfur Batteries. *Adv. Energy Mater.* **2020,** 10, 1904273-1904285.
34. Wang, M.; Fan, L.; Sun, X.; Guan, B.; Jiang, B.; Wu, X.; Tian, D.; Sun, K.; Qiu, Y.; Yin, X.; Zhang, Y.; Zhang, N. Nitrogen-Doped CoSe2 as a Bifunctional Catalyst for High Areal Capacity and Lean Electrolyte of Li–S Battery. *ACS Energy Lett.* **2020,** 5, 3041-3050.
35. Chen, L.; Xu, Y.; Cao, G.; Sari, H. M. K.; Duan, R.; Wang, J.; Xie, C.; Li, W.; Li, X. Bifunctional Catalytic Effect of CoSe2 for Lithium–Sulfur Batteries: Single Doping versus Dual Doping. *Adv. Funct. Mater.* **2021,** 32, 2107838-2107850.
36. Yang, D.; Zhang, C.; Biendicho, J. J.; Han, X.; Liang, Z.; Du, R.; Li, M.; Li, J.; Arbiol, J.; Llorca, J.; Zhou, Y.; Morante, J. R.; Cabot, A. ZnSe/N-Doped Carbon Nanoreactor with Multiple Adsorption Sites for Stable Lithium-Sulfur Batteries. *ACS Nano* **2020,** 14, 15492-15504.
37. Yuan, Z.; Peng, H. J.; Hou, T. Z.; Huang, J. Q.; Chen, C. M.; Wang, D. W.; Cheng, X. B.; Wei, F.; Zhang, Q. Powering Lithium-Sulfur Battery Performance by Propelling Polysulfide Redox at Sulfiphilic Hosts. *Nano Lett.* **2016,** 16, 519-527.
38. Pu, J.; Shen, Z.; Zheng, J.; Wu, W.; Zhu, C.; Zhou, Q.; Zhang, H.; Pan, F. Multifunctional Co 3 S 4 @sulfur nanotubes for enhanced lithium-sulfur battery performance.

Nano Energy **2017,** 37, 7-14.
39. Yuan, H.; Peng, H.-J.; Li, B.-Q.; Xie, J.; Kong, L.; Zhao, M.; Chen, X.; Huang, J.-Q.; Zhang, Q. Conductive and Catalytic Triple-Phase Interfaces Enabling Uniform Nucleation in High-Rate Lithium-Sulfur Batteries. *Adv. Energy Mater.* **2019,** 9, 1802768-1802776.
40. Ye, Z.; Jiang, Y.; Li, L.; Wu, F.; Chen, R. Self-Assembly of 0D-2D Heterostructure Electrocatalyst from MOF and MXene for Boosted Lithium Polysulfide Conversion Reaction. *Adv. Mater.* **2021,** 33, 2101204-2101215.
41. Xie, Y.; Cao, J.; Wang, X.; Li, W.; Deng, L.; Ma, S.; Zhang, H.; Guan, C.; Huang, W. MOF-Derived Bifunctional Co0.85Se Nanoparticles Embedded in N-Doped Carbon Nanosheet Arrays as Efficient Sulfur Hosts for Lithium-Sulfur Batteries. *Nano Lett.* **2021,** 21, 8579-8586.
42. Wolverton;, A. Y. S. E. C. B. S. Y. L. E. K. Z. Y. S. K. V. V. K. J. L. C. S. J. C. Theory-guided experimental design in battery materials research. *Science Advances* 8, eabm2422-eabm2439.
43. Caban-Acevedo, M.; Faber, M. S.; Tan, Y.; Hamers, R. J.; Jin, S. Synthesis and properties of semiconducting iron pyrite (FeS2) nanowires. *Nano Lett.* **2012,** 12, 1977-82.
44. Liu, Y.; Cheng, H.; Lyu, M.; Fan, S.; Liu, Q.; Zhang, W.; Zhi, Y.; Wang, C.; Xiao, C.; Wei, S.; Ye, B.; Xie, Y. Low overpotential in vacancy-rich ultrathin CoSe2 nanosheets for water oxidation. *J. Am. Chem. Soc.* **2014,** 136, 15670-15675.
45. Wang, D.; Li, F.; Lian, R.; Xu, J.; Kan, D.; Liu, Y.; Chen, G.; Gogotsi, Y.; Wei, Y. A General Atomic Surface Modification Strategy for Improving Anchoring and Electrocatalysis Behavior of Ti3C2T2 MXene in Lithium-Sulfur Batteries. *ACS Nano* **2019,** 13, 11078-11086.
46. Ye, H.; Sun, J.; Zhang, S.; Lin, H.; Zhang, T.; Yao, Q.; Lee, J. Y. Stepwise Electrocatalysis as a Strategy against Polysulfide Shuttling in Li-S Batteries. *ACS Nano* **2019,** 13, 14208-14216.
47. Peng, L.; Wei, Z.; Wan, C.; Li, J.; Chen, Z.; Zhu, D.; Baumann, D.; Liu, H.; Allen, C. S.; Xu, X.; Kirkland, A. I.; Shakir, I.; Almutairi, Z.; Tolbert, S.; Dunn, B.; Huang, Y.; Sautet, P.; Duan, X. A fundamental look at electrocatalytic sulfur reduction reaction. *Nat. Catal.* **2020,** 3, 762-770.
48. Yang, X.; Gao, X.; Sun, Q.; Jand, S. P.; Yu, Y.; Zhao, Y.; Li, X.; Adair, K.; Kuo, L. Y.; Rohrer, J.; Liang, J.; Lin, X.; Banis, M. N.; Hu, Y.; Zhang, H.; Li, X.; Li, R.; Zhang, H.; Kaghazchi, P.; Sham, T. K.; Sun, X. Promoting the Transformation of Li2 S2 to Li2 S: Significantly Increasing Utilization of Active Materials for High-Sulfur-Loading Li-S Batteries. *Adv. Mater.* **2019,** 31, 1901220-1901230.
49. Deng, Y.; Shang, T.; Wu, Z.; Tao, Y.; Luo, C.; Liang, J.; Han, D.; Lyu, R.; Qi, C.; Lv, W.; Kang, F.; Yang, Q. H. Fast Gelation of Ti3 C2 Tx MXene Initiated by Metal Ions. *Adv. Mater.* **2019,** 31, 1902432-1902439.
50. Zeng, Z.; Fu, G.; Yang, H. B.; Yan, Y.; Chen, J.; Yu, Z.; Gao, J.; Gan, L. Y.; Liu, B.; Chen, P. Bifunctional N-CoSe2/3D-MXene as Highly Efficient and Durable Cathode for Rechargeable Zn–Air Battery. *ACS Mater. Lett.* **2019,** 1, 432-439.
51. Wyatt, B. C.; Anasori, B. Self-assembly and in-situ characterization of Ti3C2T in Al: A step toward additive manufacturing of MXene-metal composites. *Applied Materials Today* **2022,** 27, 101451-101462.
52. Yang, J.; Chen, G.-H.; Zeng, J.-H.; Yu, S.-H.; Liu, X.-M.; Qian, Y.-T. Shape Control and Characterization of Transition Metal Diselenides MSe_2 (M = Ni, Co, Fe) Prepared by a Solvothermal-Reduction Process. *Chem. Mater.* **2001,** 13, 848-853.
53. Hu, T.; Wang, J.; Zhang, H.; Li, Z.; Hu, M.; Wang, X. Vibrational properties of Ti3C2 and Ti3C2T2 (T = O, F, OH) monosheets by first-principles calculations: a comparative study. *Phys Chem Chem Phys* **2015,** 17, 9997-10003.
54. Sarycheva, A.; Makaryan, T.; Maleski, K.; Satheeshkumar, E.; Melikyan, A.;

Minassian, H.; Yoshimura, M.; Gogotsi, Y. Two-Dimensional Titanium Carbide (MXene) as Surface-Enhanced Raman Scattering Substrate. *J. Phys. Chem* **2017,** 121, 19983-19988.
55. Zhang, J.; Kong, N.; Uzun, S.; Levitt, A.; Seyedin, S.; Lynch, P. A.; Qin, S.; Han, M.; Yang, W.; Liu, J.; Wang, X.; Gogotsi, Y.; Razal, J. M. Scalable Manufacturing of Free-Standing, Strong Ti3 C2 Tx MXene Films with Outstanding Conductivity. *Adv. Mater.* **2020,** 32, 2001093-2001102.
56. Lin, H.; Zhang, S.; Zhang, T.; Cao, S.; Ye, H.; Yao, Q.; Zheng, G. W.; Lee, J. Y. A Cathode-Integrated Sulfur-Deficient Co9S8 Catalytic Interlayer for the Reutilization of "Lost" Polysulfides in Lithium-Sulfur Batteries. *ACS Nano* **2019,** 13, 7073-7082.
57. Zhou, G.; Tian, H.; Jin, Y.; Tao, X.; Liu, B.; Zhang, R.; Seh, Z. W.; Zhuo, D.; Liu, Y.; Sun, J.; Zhao, J.; Zu, C.; Wu, D. S.; Zhang, Q.; Cui, Y. Catalytic oxidation of Li2S on the surface of metal sulfides for Li-S batteries. *Proc. Natl. Acad. Sci. U S A* **2017,** 114, 840-845.
58. Elgrishi, N.; Rountree, K. J.; McCarthy, B. D.; Rountree, E. S.; Eisenhart, T. T.; Dempsey, J. L. A Practical Beginner's Guide to Cyclic Voltammetry. *J. Chem. Educ.* **2017,** 95, 197-206.
59. Li, Y.; Wang, W.; Zhang, B.; Fu, L.; Wan, M.; Li, G.; Cai, Z.; Tu, S.; Duan, X.; Seh, Z. W.; Jiang, J.; Sun, Y. Manipulating Redox Kinetics of Sulfur Species Using Mott-Schottky Electrocatalysts for Advanced Lithium-Sulfur Batteries. *Nano Lett.* **2021,** 21, 6656-6663.
60. Cai, D.; Lu, M.; Li; Cao, J.; Chen, D.; Tu, H.; Li, J.; Han, W. A Highly Conductive MOF of Graphene Analogue Ni3 (HITP)2 as a Sulfur Host for High-Performance Lithium-Sulfur Batteries. *Small* **2019,** 15, 1902605-190266.
61. Zhang, C.; Biendicho, J. J.; Zhang, T.; Du, R.; Li, J.; Yang, X.; Arbiol, J.; Zhou, Y.; Morante, J. R.; Cabot, A. Combined High Catalytic Activity and Efficient Polar Tubular Nanostructure in Urchin‐Like Metallic NiCo2Se4 for High‐Performance Lithium–Sulfur Batteries. *Adv. Funct. Mater.* **2019,** 29, 1903842-1903853.
62. Su, D.; Cortie, M.; Fan, H.; Wang, G. Prussian Blue Nanocubes with an Open Framework Structure Coated with PEDOT as High-Capacity Cathodes for Lithium-Sulfur Batteries. *Adv. Mater.* **2017,** 29, 1700587-1700595.

TOC Graphic

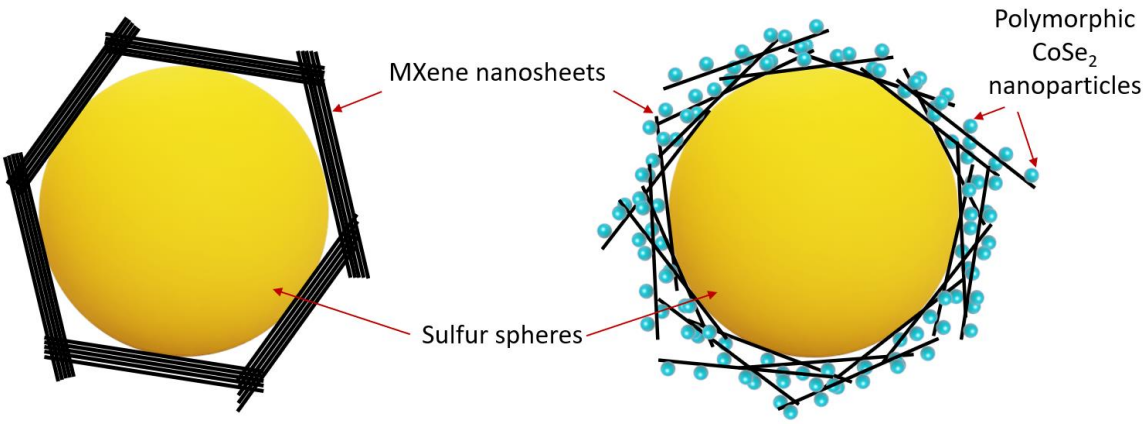

S@MXene
Well-stacked MXene nanosheets around sulfur sphere

S@MXene-$CoSe_2$
Less-orderly stacked MXene-$CoSe_2$ nanosheets around sulfur sphere